POLITECNICO DI TORINO
Repository ISTITUZIONALE

A Highway Vehicular Channel Model for OTFS Performance Evaluation

Original
A Highway Vehicular Channel Model for OTFS Performance Evaluation / Compagnoni, A., Tuninato, R., Chiasserini, C.F., Garello, R., Nordio, A., Viterbo, E.. - In: IEEE TRANSACTIONS ON COMMUNICATIONS. - ISSN 0090-6778. - 74:(2026), pp. 5074-5088. [10.1109/TCOMM.2026.3663522]

Availability:
This version is available at: 11583/3007387 since: 2026-02-12T10:08:00Z

Publisher:
IEEE

Published
DOI:10.1109/TCOMM.2026.3663522

Terms of use:

This article is made available under terms and conditions as specified in the corresponding bibliographic description in the repository

Publisher copyright
IEEE postprint/Author's Accepted Manuscript

©2026 IEEE. Personal use of this material is permitted. Permission from IEEE must be obtained for all other uses, in any current or future media, including reprinting/republishing this material for advertising or promotional purposes, creating new collecting works, for resale or lists, or reuse of any copyrighted component of this work in other works.

(Article begins on next page)

27 June 2026

A Highway Vehicular Channel Model for OTFS Performance Evaluation

A. Compagnoni, *Student Member, IEEE*, R. Tuninato, *Student Member, IEEE*, C. F. Chiasserini, *Fellow, IEEE*, R. Garello, *Senior Member, IEEE*, A. Nordio, *Member, IEEE*, and E. Viterbo, *Fellow, IEEE*

***Abstract*—In vehicular communications, accurate modeling of real-world radio propagation channels is essential. To this end, we propose a novel stochastic model, named *Vehicular-Tapped Delay-Line* (V-TDL) that accurately captures the statistical behavior of multipath channels characterized by path-dependent gains, delays, and Doppler shifts. V-TDL supports diverse traffic conditions and road geometries by generating channel instances through well-established probability distributions. Also, it effectively models the parameters of the distributions through realistic geometry-based simulations, achieving the accuracy of a ray-tracing-based model while maintaining the low complexity of a purely stochastic approach. In contrast to existing models, V-TDL accounts for the correlation between propagation paths. Our findings show that this correlation is inherent in high-speed vehicular environments and neglecting it leads to a significant overestimation of channel diversity and system performance. We compare our model to existing alternatives to assess the performance of OTFS and OFDM modulations. The results demonstrate that, unlike traditional models such as the 3GPP EVA, V-TDL captures variations in channel diversity influenced by traffic intensity and road geometry, which impact the OTFS and OFDM performance. Although OTFS is penalized by path correlation, it consistently outperforms OFDM in all evaluated vehicular environments, confirming its suitability for high-speed vehicular communication scenarios.**

***Index Terms*—Channel modeling, OTFS, 5G/6G, Connected vehicles, Mobility.**

I. Introduction

WIRELESS networks are evolving to provide connectivity in very *high-mobility* scenarios [1], [2], [3], [4]. A prominent example is represented by connected vehicles for which critical applications such as autonomous driving and safety services require reliable radio coverage and data transfer [5], [6]. In this context, knowledge of the wireless channel plays a pivotal role in system design and connectivity provisioning, as it can dramatically affect performance assessment and key decisions, such as radio points of access placement, transmit power setting, or modulation scheme selection. However, solving electromagnetic equations in real time is far too complex, particularly for highly mobile terminals. Thus, stochastic *channel models* are often used to approximate the behavior of the wireless propagation channel [7].

Stochastic models typically approximate the wireless channel through a fixed number of taps with a specific *power delay profile*. Such models are commonly referred to as *tapped delay-line* (TDL); notably, the 3GPP standard [8] defines three variants of such models tailored for environments with low, medium, and high delay. The medium delay case, represented by the Extended Vehicular A (EVA) model, is specifically designed for vehicular scenarios in urban and suburban areas [9]. Although widely used to simulate high-mobility multipath channels, EVA neither can capture the impact of varying vehicular conditions nor accounts for the correlation between propagation paths – a factor proven to be intrinsic to high-speed vehicular scenarios, which significantly affects channel diversity and system performance [10].

Alternative approaches utilize ray-tracing simulators, which accurately characterize signal propagation by leveraging electromagnetic and optical theory [11], [12], [13]. Ray tracing-based models, while accurate, are often computationally intensive and highly specific to the scenario being considered, making them less suitable for designing and evaluating system performance across diverse environments. This highlights the ongoing need for a vehicular channel model that provides both accuracy and flexibility to accommodate different road geometries and traffic scenarios.

It is also worth noting that channel models suitable for high-mobility network scenarios are essential to evaluate the performance of modulation schemes such as orthogonal time frequency space (OTFS) modulation or orthogonal frequency division modulation (OFDM). The former has recently emerged as a very effective scheme, especially in vehicular scenarios where multipath propagation and large Doppler shifts degrade the performance of traditional OFDM modulation due to significant inter-carrier interference [14], [15], [16], [17], [18], [19], [20], [21], [22], [23]. Since OTFS operates in the delay-Doppler domain, it takes advantage of the sparser representation of high-mobility channels. However, the full advantages of OTFS over OFDM in vehicular environments remain unclear, as most studies in the literature evaluating OTFS rely primarily on the simple EVA channel model.

In this work, we propose a novel channel model, referred to as *Vehicular Tapped Delay-Line (V-TDL)* model, specifically tailored for vehicular communication. Our V-TDL model *(i)*

A. Compagnoni, C. F. Chiasserini, R. Garello, and R. Tuninato are with Politecnico di Torino, Torino, Italy. C. F. Chiasserini and R. Garello are also with CNIT, Parma, Italy. A. Nordio is with CNR-IEIIT, Torino, Italy. E. Viterbo is with ECSE, Monash University, Clayton, Australia.

This work was funded by the SNS JU under the EU's Horizon Europe research and innovation programme under the MultiX project Grant Agreement No. 101192521, and by the EU - Next Generation EU under the Italian National Recovery and Resilience Plan (NRRP), Mission 4, Component 2, Investment 1.3, CUP E13C22001870001, partnership on "Telecommunications of the Future" (PE00000001 - program "RESTART") and within the CSI-Future project under the PRIN 2022 PNRR program (D.D.1409 del 14/09/2022 MUR). This manuscript reflects only the authors' views and opinions and the Ministry cannot be considered responsible for them. The work of E. Viterbo was supported by the Australian Research Council (ARC) through the Discovery project: DP200100096. Email: alessandro.compagnoni@polito.it

offers accuracy comparable to ray-tracing-based models, *(ii)* is as simple to implement as a tapped delay-line model such as EVA, and *(iii)* provides high flexibility, enabling tunable traffic intensity and road geometry. Furthermore, thanks to its ability to accurately model real-world channels in highly mobile scenarios, our channel model can be used to assess the performance of OTFS and OFDM modulation schemes in real-world vehicular environments.

Our main contributions are thus as follows:

- *Statistical analysis:* We start from the V-CORE model, a realistic geometry-based stochastic model whose main feature is the characterization of channel gains based on the bistatic radar cross section of the reflective vehicles [10]. We perform a statistical analysis of V-CORE under typical highway environments, considering different road geometries and vehicle traffic intensities. Specifically, we collect relevant statistics for delays, Doppler shifts, and channel gains resulting from signal reflections caused by other vehicles. We show that the propagation paths in high-speed vehicular scenarios are *highly correlated* – an aspect neglected in other models (like the popular EVA model) – that leads to an overestimation of the OTFS performance.
- *Characterization of the new V-TDL channel model:* We use the results of our extensive statistical analysis of V-CORE to develop V-TDL, a new flexible vehicular channel model capable of generating realistic instances of delays, Doppler shifts, number of paths, and channel coefficients across different signal propagation paths.
- *OTFS vs. OFDM over V-TDL and EVA models:* We evaluate the performance of OTFS and OFDM modulation schemes under both the 3GPP EVA model and our proposed V-TDL model. Unlike EVA, V-TDL accurately represents the correlation between paths and, as a direct consequence, captures the relationship between vehicular traffic intensity and channel diversity. We show that OTFS and OFDM exhibit opposite performance trends: as traffic increases, OTFS benefits from high channel diversity, whereas OFDM suffers due to inter-carrier interference. Although the EVA model overestimates OTFS performance, OTFS still outperforms OFDM even under V-TDL, confirming OTFS's suitability for vehicular communications.
- *V-TDL vs. V-CORE:* We show that the performance under the proposed V-TDL tapped delay-line statistical model closely matches that of V-CORE geometry-based stochastic model under comparable traffic conditions. Importantly, unlike V-CORE, V-TDL does not require populating the road, solving ray-tracing equations for multiple propagation paths (by computing the bistatic radar cross section for all reflectors). Instead, V-TDL is designed to generate channel instances based on simple probability distributions, making it easier to implement, less computationally expensive, and more flexible for exploring a wide range of traffic scenarios, while still capturing the correlation between multipath components.
- *Channel diversity and OTFS performance:* Finally, we analyze how channel diversity is affected by different degrees of correlation between multipath components and by different system bandwidths. We then show how this diversity affects the OTFS performance.

The remainder of the paper is organized as follows. Section II discusses relevant related work while highlighting the novelty of our study. Section III introduces our notation as well as some background on time-varying multipath channels and on the V-CORE channel model. Section IV presents a statistical analysis of V-CORE, which serves as a basis for developing the proposed V-TDL model. Our main contribution is presented in Section V, where we describe and analyze our V-TDL model. Section VI compares V-TDL against the V-CORE and the 3GPP EVA model, evaluating the performance of OFDM and OTFS, and analyzing how the latter is affected by different degrees of correlation between multipath components as well as by varying values of bandwidth. Finally, we draw our conclusions in Section VII.

II. Related Work

Our work primarily relates to the areas of channel characterization and modeling in vehicular scenarios, and of OTFS performance in such environments.

Vehicular Channel Characterization and Modeling. Concerning communication channel in vehicular scenarios, and specifically in highway environments, [24] presents the results of a measurement campaign conducted in Lund, Sweden, capturing vehicle-to-vehicle (V2V) channel parameters including delay spread, power delay profiles, and delay-Doppler spectra. Although the methodology used in this study involves real-world channel measurements – which are generally considered reliable – it is often an expensive approach, which is also specific to the measured environment.

A more practical methodology involves the use of ray-based models, such as ray-launching (RL) and ray-tracing (RT) models. The study in [25] leverages RL simulations to compare the performance of OTFS and OFDM in vehicle-to-infrastructure communication scenarios. [26] investigates, instead, V2V communication in high-traffic urban settings, deriving key channel characteristics such as delay spread and path loss distribution through RT simulations. Similarly, [27] analyzes an urban intersection scenario, demonstrating a strong correlation between RT-derived power delay profiles and real-world sounder measurements. While RT simulators suffer from high computational complexity, RL methods are less complex and more cost-effective than both channel sounding measurements and RT models, although they yield less realistic results.

Other studies focus on geometry-based stochastic channel models (GBSCMs), in which reflectors are positioned according to a probability distribution and the received signal is computed as the sum of ray-tracing solutions from each reflecting component. Among these, [28] introduces a GBSCM for MIMO (Multiple Input Multiple Output)-based V2V communication, while [29] analyzes vehicular channels through the theory of ambit processes to enable fast simulations and improve the spatial consistency of multipath propagation. [30] proposes a GBSCM for V2V visible light communication, characterizing a direct path and a reflected path from another vehicle, assuming a Lambertian radiation pattern. The work in [31], instead, proposes a GBSCM that leverages a sum-of-sinusoids simulation model for a MIMO V2V Rician fading channel. Its main features include a distinction between

moving vehicles (two-sphere representation) and the stationary environment (elliptic-cylinder model). [32] proposes a V2V channel representation in the delay-Doppler domain using a GBSCM, where they model the V2V channel impulse response considering reflections from the ground, moving vehicles, static reflectors, and diffuse components.

In [10], we introduced a GBSCM called V-CORE, specifically designed for vehicular scenarios. A distinguishing feature of V-CORE is its bistatic radar cross section modeling of multiple reflective vehicles, which provides a realistic representation of channel gains across different scenario realizations. We remark that GBSCMs represent a more flexible and less computationally expensive approach compared to ray-based models. However, they are still more complex and less practical than purely stochastic models.

OTFS Performance in Vehicular Environments. Our work is particularly relevant to the study of OTFS-modulated systems (a useful overview of OTFS and its variants can be found in [33]). While a large body of work has investigated the performance of OTFS, fewer have tackled this challenge in vehicular scenarios. Among these, [34] analyzes vehicular channels using mmWave measurements at vehicular crossroads, assessing sparsity in the delay-Doppler domain. An urban scenario is considered also in [35], which evaluates OTFS performance over vehicular communication channels measured in Vienna, demonstrating that OTFS outperforms OFDM under strong multipath conditions. Conversely, [36] presents a vehicular mmWave measurement campaign, comparing various OTFS-based channel estimation techniques in an indoor car park environment. In [37], low-complexity zero-forcing and minimum mean square error receivers are designed for MIMO-OTFS systems in high-speed vehicular communications. On the other hand, [38] focuses on OTFS for vehicular IoT networks, proposing an embedded pilot design in the Delay-Doppler domain to optimize spectral efficiency based on vehicle speed. Finally, [39] investigates an OTFS-based sparse code multiple access (SCMA) system in an uplink coordinated multi-point vehicle communications, exploiting positive and negative Doppler shifts to enhance diversity.

Novelty. Unlike previous work, we develop a channel model for high-speed vehicular scenarios, which exhibits the accuracy level typical of RT-based models while retaining the low complexity and flexibility typical of stochastic and GBSCM models. Also, our model can accurately capture the impact of channel diversity on system performance, thereby enabling a fair assessment of the advantages of OTFS over OFDM.

III. Preliminaries

This section first introduces some notation that we will use throughout the paper (Section III-A). Then it provides the necessary background on time-varying channels and OTFS modulation (Section III-B), as well as on the V-CORE channel model (Section III-C).

A. Notation

The transpose and Hermitian transpose of a matrix $\mathbf{A}$ are denoted by $\mathbf{A}^{\mathsf{T}}$ and $\mathbf{A}^{\dagger}$ (resp.). The (m,n)-th element of the matrix $\mathbf{A}$ is denoted by $\mathbf{A}(m,n)$. The operation $\mathrm{vec}(\mathbf{A})$ refers to the column-wise vectorization of the matrix $\mathbf{A}$, and $\mathrm{vec}^{-1}_{M,N}(\mathbf{a})$ refers to the matrix formed by column-wise folding a vector $\mathbf{a}$ into a matrix $M\times N$. The matrix $\mathbf{F}_N$ represents the N-point normalized discrete Fourier Transform (DFT), with its (i,k)-th element given by $\mathbf{F}_N(i,k)=\mathrm{e}^{-\mathrm{j}2\pi ik/N}/\sqrt{N}$. The probability that a random variable X takes the value x is denoted by $\mathbb{P}(X=x)$, and the expectation operator by $\mathbb{E}[\cdot]$. The integer round operator is denoted by $\lfloor\cdot\rceil$. Finally, $|\mathbf{a}_1-\mathbf{a}_2|$ denotes the Euclidean distance between the vectors $\mathbf{a}_1$ and $\mathbf{a}_2$.

B. Time-Varying Multipath Channels and OTFS

Since our focus is on vehicular communication, we consider scenarios that involve multiple scatterers moving relatively to a receiver. This leads to the generation of multiple signal echos subject to different delays and Doppler shifts. We consider P scatterers that generate propagation paths, where the i-th path, for $i=1,\dots,P$, can be characterized in the complex baseband representation by a channel coefficient h_i, a delay τ_i, and a Doppler shift ν_i. Given these parameters, the channel response in the *delay-Doppler* domain is expressed as [40]:

$$h(\tau,\nu)=\sum_{i=1}^{P} h_i\,\delta(\tau-\tau_i)\,\delta(\nu-\nu_i)\,. \tag{1}$$

This *delay-Doppler* representation is particularly well-suited for modeling high-mobility multipath fading, as it explicitly highlights the effects of both path delays and Doppler shifts, which, along with the channel gains, fully describe the channel. Moreover, small-scale fading is typically characterized by a limited number of paths P around the receiver, which makes the delay-Doppler representation inherently sparse.

Finally, we note that the *delay-Doppler* response in (1) is directly related to other conventional channel representations. Specifically, it can be derived from the *delay-time* channel response through the Fourier transform along the time axis, and from the *frequency-time* response through the two-dimensional symplectic Fourier transforms (see [23] for details).

In OTFS, symbols are placed on the $M\times N$ delay-Doppler grid, with M representing the number of *delay bins* and N the number of *Doppler bins*, forming the delay-Doppler domain signal $\mathbf{X}_{\mathrm{dd}}\in\mathbb{C}^{M\times N}$. From the delay-Doppler domain, the transmitted time-domain vector $\mathbf{s}\in\mathbb{C}^{MN\times 1}$ is obtained by applying the *Inverse Discrete Zak Transform (IDZT)* [23]:

$$\mathbf{s}=\mathrm{IDZT}\{\mathbf{X}_{\mathrm{dd}}\}=\mathrm{vec}(\mathbf{X}_{\mathrm{dd}}\mathbf{F}_N^{\dagger})\,. \tag{2}$$

The received signal is transformed into the delay-time domain:

$$\mathbf{Y}_{\mathrm{dt}}=\mathrm{vec}^{-1}_{M,N}(\mathbf{r})\in\mathbb{C}^{M\times N} \tag{3}$$

where $\mathbf{r}\in\mathbb{C}^{M\times N}$ is the received sampled signal. The delay-time domain allows for an optimal trade-off between performance and complexity when using the *Zero-Padding (ZP)* variant of OTFS with *Maximum Ratio Combining (MRC)* detection method, as described in [41].

If we consider the channel response in (1) with distinct Doppler shift values ν_i across the paths $i=1,\dots,P$, then the traditional OFDM modulation scheme suffers from ICI. In contrast, OTFS can exploit such channel diversity by

coherently combining the different propagation paths resolved in the *delay-Doppler* domain.

C. V-CORE Channel Model

Next, we provide an overview of the V-CORE channel model, a geometry-based stochastic channel model designed for vehicular scenarios. For a more extensive explanation of V-CORE, the reader can refer to our work detailed in [10].

The model considers a downlink scenario where a Point of Access (PoA) is positioned at the center of a highway-like environment, transmitting to a receiving vehicle, which, for simplicity, we will refer to as RX. The V-CORE model aims to characterize the delay, Doppler shift, and channel gain of multiple reflections induced by surrounding vehicles.

These vehicles enter lane $\ell{=}1,\dots,N_L$ according to a Poisson point arrival process with an arrival rate ρ_ℓ. The lane index $\ell{=}1$ represents the outermost (slowest) lane, while $\ell{=}N_L$ denotes the innermost (fastest) lane. Each vehicle on lane ℓ moves at a random velocity v following a uniform distribution $U(v_\ell^{\min}, v_\ell^{\max})$, where $v_\ell^{\min}$ and $v_\ell^{\max}$ define the minimum and maximum speeds for that lane.

TABLE I: Default V-CORE parameters

PARAMETER	VALUE
Number of lanes, N_L	3
Minimum velocity in each lane, $v_\ell^{\min}$	{70, 100, 130} km/h
Maximum velocity in each lane, $v_\ell^{\max}$	{100, 130, 160} km/h
Vehicle length in each lane, L_ℓ	{16.0, 6.0, 4.4} m
Average distance between vehicles, μ_d	80 m
Safety distance between vehicles, D_s	20 m
Lane width, W	4 m
Space between travel directions, D_t	2 m
Minimum PoA-RX distance, $d_{\min}$	50 m
Maximum PoA-RX distance, $d_{\max}$	700 m

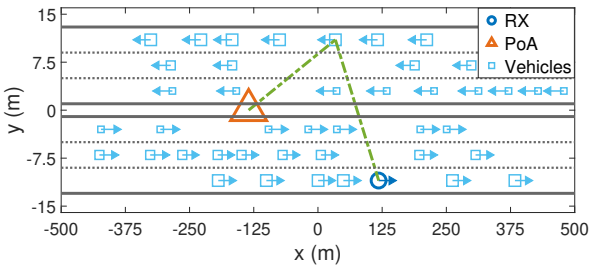

Fig. 1: Road scenario and example of an nLoS path (green dashed line) generated by a reflecting vehicle.

Table I shows an example of the V-CORE input parameters, while Fig. 1 depicts an example of a V-CORE scenario realization.

For simplicity, the direct line-of-sight (LoS) path is denoted with $i{=}1$, while non-line-of-sight (nLoS) paths are indexed as $i{=}2,\dots,P$. The delay and Doppler shift for the LoS path are given by:

$$\tau_1{=}\frac{d_1}{c}, \quad \nu_1{=}\frac{1}{\lambda_c}\mathbf{v}_1^{\mathsf{T}}\frac{\mathbf{p}_\mathrm{A}-\mathbf{p}_1}{d_1} \tag{4}$$

where $d_1{=}|\mathbf{p}_\mathrm{A}-\mathbf{p}_1|$ represents the distance between the PoA and RX, with $\mathbf{p}_\mathrm{A}$ and $\mathbf{p}_1$ denoting their respective position vectors. The RX's velocity vector is $\mathbf{v}_1$, while $\lambda_c{=}c/f_c$ is the signal wavelength, where f_c is the carrier frequency and c is the speed of light.

For nLoS paths ($i{=}2,\dots,P$), V-CORE adopts a *bistatic radar* model, where the PoA serves as the transmitter, the receiving vehicle as the receiver, and other vehicles as reflecting targets. The delay of a reflected path is given by $\tau_i{=}d_i/c$ where $d_i{=}|\mathbf{p}_\mathrm{A}-\mathbf{p}_i|+|\mathbf{p}_i-\mathbf{p}_1|$ represents the total signal travel distance from the PoA to RX via the reflecting vehicle at position $\mathbf{p}_i$. In a bistatic radar system, the observed Doppler shift at the receiver depends on the sum of the transmitter's velocity relative to the target and the target's velocity relative to the receiver [42, Ch. 6] and can be expressed as:

$$\nu_i{=}\frac{1}{\lambda_c}\left[\mathbf{v}_i^{\mathsf{T}}\frac{\mathbf{p}_\mathrm{A}-\mathbf{p}_i}{|\mathbf{p}_\mathrm{A}-\mathbf{p}_i|}+(\mathbf{v}_1-\mathbf{v}_i)^{\mathsf{T}}\frac{\mathbf{p}_i-\mathbf{p}_1}{|\mathbf{p}_i-\mathbf{p}_1|}\right],\ i{=}2,\dots,P \tag{5}$$

where $\mathbf{v}_i$ is the velocity vector of the reflecting vehicle i.

To account for signal attenuation in the nLoS paths, the model exploits the *bistatic radar cross section* (RCS) of the reflecting vehicle, which quantifies the effective area (in m^2) that intercepts and redirects the transmitted signal toward the receiver. The bistatic RCS $\psi_i{=}f(\theta_i^{\mathrm{PoA}},\theta_i^{\mathrm{RX}},f_c)$ depends on the signal frequency f_c and the angles of arrival θ_i^{PoA} and departure θ_i^{RX} [43]. Consequently, the complex channel coefficient for an nLoS path is given by [44, Sec. 4–6]:

$$h_i{=}\frac{\lambda_c \mathrm{e}^{\mathrm{j}\phi_i}}{(4\pi)^2|\mathbf{p}_\mathrm{A}-\mathbf{p}_i|\cdot|\mathbf{p}_i-\mathbf{p}_1|}\sqrt{4\pi\psi_i G_\mathrm{A}G_\mathrm{R}} \tag{6}$$

where G_A and G_R denote the antenna gains of the PoA and RX, respectively, and $\phi_i \sim U(0,2\pi)$ represents the random phase shift of the i-th path. Regarding the LoS path, the channel coefficient is assumed to follow $h_1 \sim \mathcal{CN}(0,1)$, and the transmit power P_{Tx} is adjusted to guarantee a 0 dB-path loss $(P_{\mathrm{Rx}}/P_{\mathrm{Tx}})$ [10].

We showed that our V-CORE model provides realistic instances of (τ_i,ν_i,h_i) needed to characterize a highly mobile vehicular channel. Next, we present a detailed statistical analysis of V-CORE, with the primary objective of demonstrating the strong correlation among propagation paths – an inherent characteristic of vehicular scenarios – and laying the groundwork for the development of our proposed V-TDL model, which constitutes the main contribution of this paper.

IV. Statistical Analysis of V-CORE

To develop the V-TDL statistical model, we first perform a thorough statistical analysis of the V-CORE model, focusing on the distribution of Doppler shifts, delays, and channel gains for each multipath component. We then quantify how these distributions are affected by different traffic intensities and road geometries. Below, we detail the steps of our analysis.

1) Average Number of Paths: As the first step, we consider the vehicular traffic environment illustrated in Table I and simulate a number of traffic scenarios using V-CORE. By doing so, we estimate the value of the average number of paths, $\mathbb{E}[P]$, then round it to the nearest integer, $\lfloor\mathbb{E}[P]\rceil$, which resulted in 28 paths. Thus, consistently with the existing Tapped Delay-Line models where the number of reflected paths is fixed, we only collect the statistics of those scenario realizations that generate a number of paths equal to the average. Henceforth, to avoid confusion, we will always denote $\lfloor\mathbb{E}[P]\rceil$ as P. The

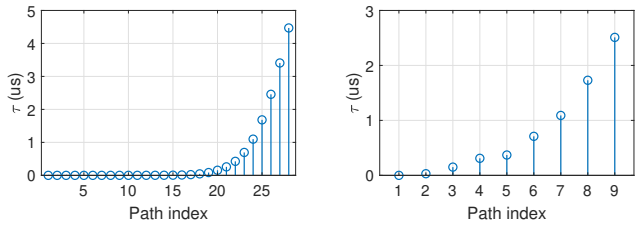

(a) V-CORE (b) EVA

Fig. 2: Average delay of different paths.

multipath components are then ordered by increasing delay, with the P-th path having the largest delay.

2) Average Delay of Paths: Next, we estimate the average delays of the different paths $1, \ldots, P$, and compare them to the delays of the EVA model. Where the LoS path delay has been subtracted from all the path delays, since the receiver is assumed to be synchronized on the LoS path. Figures 2a and 2b show such delays for the V-CORE model and the EVA model, respectively.

One can observe that, approximately, the first 16 paths of V-CORE exhibit (almost) the same delay. These paths come from vehicles that are very close to the RX or very close to the PoA, resulting in delays almost equal to 0, i.e., that of the LoS. Furthermore, traveling over a short distance, such paths are also the ones associated with higher energy. As better detailed next, this leads to a significant correlation between paths in highway scenarios. Then, looking at the paths from 17 onward, the average delay increases exponentially, eventually reaching approximately 4,5 μs for the P-th path.

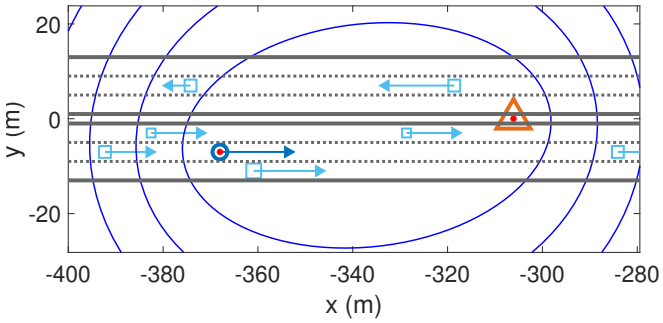

Fig. 3: Delay bins observed by the receiver represented by concentric ellipses.

Fig. 3, obtained for a generic scenario realization, underlines how different vehicles can be mapped into different delay bins. The figure depicts several ellipses, with vehicles comprised between two concentric ellipses falling into the same delay bin. These ellipses with foci PoA and RX represent the location of scatterers generating paths with the same delay. This implies that the receiver cannot distinguish among the delays of reflected paths that come from those vehicles. The delay resolution represented in the figure has been determined using M=512 and subcarrier spacing Δf=30 kHz, which translates to a path length resolution of $c/(M\Delta f)$≈19.5 m, which is smaller than the inter-vehicular safety distance between cars travelling on the same lane. However, cars in adjacent lanes may have a smaller separation, and, hence, their associated paths are not mutually resolved in the delay domain. Furthermore, it is worth noticing that several vehicles fall within the first two ellipses (corresponding to the smallest delay values), confirming that shorter paths, with small delays, exhibit similar characteristics. Vehicles falling within the same ellipse also form a very similar angle between the PoA and the OBU, thereby introducing correlation in the Doppler shift, as discussed in Sec. IV-5.

At last, we remark that, unlike in the V-CORE case, according to the EVA model, almost all paths are associated with well-distinguished values of delay, thus providing a channel diversity higher than what observed in Fig. 3 and expected in a real-world vehicular scenario.

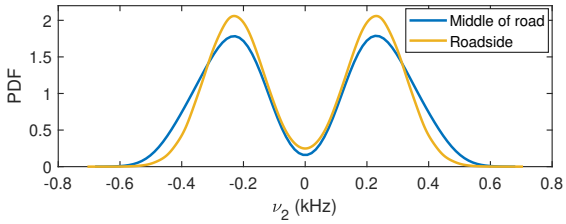

Fig. 4: Estimated Doppler shift distribution of a representative reflected (nLoS) path.

3) Doppler Distribution: Fig. 4 shows the estimated Doppler shift distribution for the first nLoS component (path number 2). The blue curve corresponds to the scenario where the PoA is located at the center of the road, while the yellow curve represents the case where the PoA is positioned along the road. The two distributions are quite similar, with only a minor difference in their variance.

These results demonstrate that the Doppler shift of a typical reflected path can be accurately modeled by using a bimodal Gaussian distribution. We remark that, although only the second path is shown here, the Doppler shift distribution of the other reflected paths exhibit similar bimodal shapes.

This result highlights *an important difference of the V-CORE compared to the EVA model*, which, as previously mentioned, assumes the Doppler shift to follow Jakes' distribution. Unlike urban environments, in a highway scenario, where typically there are no walls or large buildings, reflections are mainly due to other vehicles. Therefore, the angles of the propagation paths with respect to the receiver are clearly not uniformly distributed, rendering the Jakes' spectrum unsuitable for describing the Doppler shift. The bimodality shown by the Doppler shift distribution in V-CORE (Fig. 4) is given by a mixture of two Gaussian distributions, with equal weights: the Gaussian on the right represents scenarios where the receiver is approaching the PoA, while the Gaussian on the left corresponds to those scenarios where the receiver is moving away from the PoA. Since both cases occur with the same probability, the weights of the two distributions composing the mixture are both equal to 0.5. Moreover, by looking at Fig. 4, it is evident that when the receiving vehicle approaches the PoA, the distribution support mainly encompasses positive values, while the opposite holds when the vehicle is getting farther away from the PoA.

We highlight that, in our model, we consider two-way traffic directions. Nevertheless, we verified that this bimodal behavior is still present in the case of one travel direction only. This is indeed consistent with the fact that, as mentioned, the bimodality of the Doppler shift distribution is due to the OBU traveling either toward the PoA or away from the PoA across different realizations.

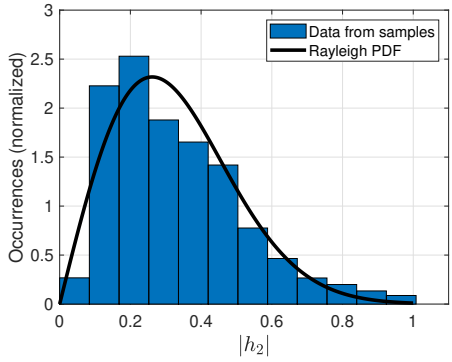

Fig. 5: Channel magnitude histogram of a representative propagation path.

4) Channel Distribution: Fig. 5 presents the channel magnitude histogram of a representative path (again, we consider the first nLoS path, i.e., the 2nd path). One can notice that the distribution resembles a Rayleigh distribution. In other words, a generic complex channel coefficient can be described by a circularly symmetric complex Gaussian distribution. It can be noticed from Fig. 5 that the magnitude is upper bounded by 1 since V-CORE sets the path loss of the LoS at 1 (0 dB), and the gain of a generic reflected path evaluated through the bistatic RCS cannot carry more power than its corresponding free-space path loss (FSPL). Since the FSPL of a reflected path is always smaller than that of the LoS, the magnitude of any channel coefficient is also bounded by 1. We underline that this does not imply that the magnitude of the channel coefficient of the LoS is always greater than that of the reflected paths. This is due to the fact that the $h_1 \sim \mathcal{CN}(0,1)$, i.e., its magnitude is Rayleigh distributed, and, of course, can take values smaller than those given by the FSPL or the RCS-based loss in (6).

5) Correlation Among Paths: The TDL models that have been proposed in the literature generally assume that each propagation path is independent of the others. However, in high-speed vehicular environments, we expect a high degree of correlation among paths, particularly from closely located reflective vehicles. Thus, we aim to demonstrate that, in a highway environment, both Doppler shifts and, to a lesser extent, channel gains, exhibit significant correlation across different paths, especially those associated with shorter delays.

To investigate this correlation, we empirically estimate the Pearson correlation matrix for both Doppler shift and channel gain samples. In our default scenario, with an expected number of paths P=28, the correlation in Doppler shifts among approximately the first 16 paths is indeed evident, as highlighted in Fig. 6, which depicts the estimated Pearson correlation matrix for the Doppler shifts across different paths. Although this observation has been made by analyzing only the scenarios where the receiver is approaching the PoA, we remark that the scenarios where the receiving vehicle is departing from the PoA yielded the same Pearson correlation matrix. Measurement campaigns have also suggested correlation among multipath components in vehicular scenarios. In particular, [45] shows that Doppler profiles associated with closely spaced delay bins have very similar shapes.

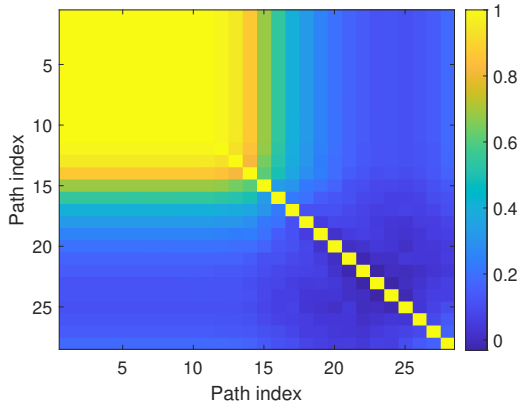

Fig. 6: Pearson correlation matrix of Doppler shifts across different propagation paths.

The Pearson correlation matrix is also presented for the channel gains of different paths in Fig. 7. The result reveals a non-negligible correlation among the first 10 paths, even though the level of correlation is much lower than that observed above for the Doppler shifts.

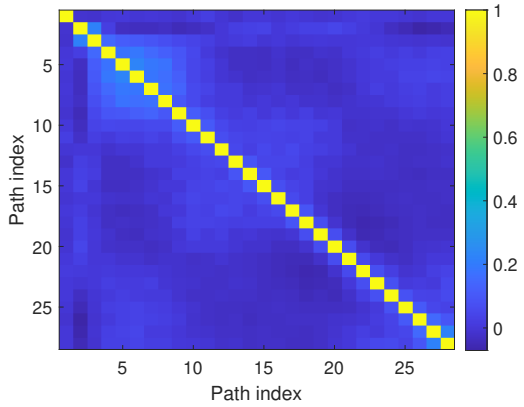

Fig. 7: Pearson correlation matrix of channel gains across different propagation paths.

The high correlation of Doppler shifts across paths reduces channel diversity, highlighting that, as mentioned, reflected components in high-mobility vehicular scenarios are inherently correlated. Therefore, *models like EVA, in which all paths are independent, are unsuitable for highway scenarios*.

In conclusion, to highlight our findings, we summarize in Table II the key differences we observed between the V-CORE and the EVA model.

V. The V-TDL Model

We now introduce the proposed Vehicular-Tapped Delay-Line (V-TDL) model, tailored specifically for high-mobility

TABLE II: Comparison between EVA and V-CORE

Feature	EVA	V-CORE
Doppler shift distribution	Jakes	Gaussian
Channel magnitude distribution	Rayleigh	Rayleigh
Correlation of Doppler between paths	No	High
Correlation of Gains between paths	No	Low

vehicular scenarios. Building on the statistical analysis of the V-CORE, the GBSCM model (see Section IV), our V-TDL model (i) aims to achieve the same high level of accuracy as a geometric model, while (ii) retaining the same level of implementation and use simplicity as a stochastic model.

Based on the results obtained through our analysis presented above, we design V-TDL in such a way that it generates channel realizations where the delays of different paths are fixed. Instead, Doppler shifts and channel coefficients follow a multivariate Gaussian distribution, accounting for the correlation among the multipath components. Below, we specify how these distributions are modeled and how they are influenced by the vehicular traffic scenario and road geometry parameters.

A. Collection of Statistics from the V-CORE Model

We collect samples of paths delays, Doppler shifts, and channel coefficients using the V-CORE channel model under 27 different configurations. Such configurations are given by all possible combinations of three system parameters, namely, the carrier frequency f_c, the average inter-vehicle distance μ_d, and the number of lanes N_L, each taking three distinct values (see Table III). Then, for each triplet (f_c, μ_d, N_L), we use the collected samples to empirically estimate the corresponding distributions of delays, Doppler shifts, and channel gains of the different multipath components. Specifically, we characterize how these distributions and their mean and covariance matrix depend on the triplet (f_c, μ_d, N_L). This final step yields the V-TDL model, which enables the generation of the multipath channel given any input triplet (f_c, μ_d, N_L). We validate our model by comparing the distributions generated by V-TDL with those empirically estimated under the same traffic conditions (i.e., values taken on by the (f_c, μ_d, N_L) parameters).

TABLE III: V-CORE input parameters

f_c	μ_d	N_L
2 GHz	30 m	1
3 GHz	110 m	3
4 GHz	190 m	5

During the samples collection, independently from the triplet (f_c, μ_d, N_L), vehicle velocities vary between 70 and 160 km/h. Specifically, on lane $\ell \in \{1, \ldots, N_L\}$, they are randomly extracted following the uniform distribution $U(v_\ell^{(\min)}, v_\ell^{(\max)})$ where

$$v_\ell^{(\min)} = \begin{cases} 70\,\text{km/h} & \text{if } N_L=1 \\ \frac{\ell-1}{N_L-1} \cdot 60 + 70\,\text{km/h} & \text{otherwise} \end{cases} \tag{7}$$

and

$$v_\ell^{(\max)} = \begin{cases} 160\,\text{km/h} & \text{if } N_L=1 \\ v_\ell^{(\min)} + 30\,\text{km/h} & \text{otherwise.} \end{cases} \tag{8}$$

As the size of the vehicle influences the bistatic RCS, we account for the vehicle's length, i.e., the dimension along its main axis. Let L_ℓ be the length of a vehicle traveling on lane ℓ and $\Delta = \{16.0, 6.0, 4.4\}$ m the set of possible vehicle lengths. Then L_ℓ is drawn according to the following probabilities:

$$\mathbb{P}(L_\ell = \Delta(i)) = \begin{cases} 0.2 \cdot N_L & \text{if } i=1 \\ 0.5 \cdot (1 - 0.2 \cdot N_L) & \text{if } i \in \{2,3\} \end{cases} \tag{9}$$

if $\ell=1$,

$$\mathbb{P}(L_\ell = \Delta(i)) = \begin{cases} 0 & \text{if } i=1 \\ 0.5 & \text{if } i \in \{2,3\} \end{cases} \tag{10}$$

if $\ell > 1$. We thus obtain that, on average, 20% of the vehicles have the maximum length, representing large trucks, and they can only travel on the first (i.e., the slowest) lane. All the other road parameters are set as indicated in Table I.

Once samples from different scenarios are collected, we use them to develop the V-TDL model, as detailed next.

B. Modeling Doppler Shifts

We start by modeling the Doppler shift distribution within V-TDL. For simplicity, we consider the case in which the receiver approaches the PoA (the case where the receiver moves away from the PoA provides symmetric results).

Let us denote by $\boldsymbol{\nu}_+ \in \mathbb{R}^P$ the Doppler shift vector, whose component $\boldsymbol{\nu}_+(p)$, for $p=1, \ldots, P$, represents the Doppler shift of the p-th propagation path.

As previously mentioned, the Doppler shift obtained through the V-CORE model is well approximated by a Multivariate Gaussian distribution. Thus, $\boldsymbol{\nu}_+$ can be modeled as:

$$\boldsymbol{\nu}_+ \sim \mathcal{N}(\boldsymbol{\mu}_\nu, \boldsymbol{\Sigma}_\nu) \tag{11}$$

where $\boldsymbol{\mu}_\nu \in \mathbb{R}^P$ is the mean vector, and $\boldsymbol{\Sigma}_\nu \in \mathbb{R}^{P \times P}$ is the covariance matrix.

To characterize the mean vector and the covariance matrix, we first analyze the average Doppler of the LoS path, i.e., $\boldsymbol{\mu}_\nu(1)$. Fig. 8 shows (solid lines) the estimated Average Doppler shift of the LoS path. As expected, the Doppler shift increases linearly with the carrier frequency.

Therefore, we can express $\boldsymbol{\mu}_\nu(1)$ as $a \cdot f_c$, where the angular coefficient a depends on the average distance between vehicles, μ_d, and the number of lanes, N_L. It is important to note that the intercept is zero since we expect the Doppler shift to be zero when the carrier frequency is zero.

We adopt a second-degree polynomial regression to model the estimated curves, expressing the angular coefficient as:

$$a = p_1 + p_2 N_L + p_3 \mu_d + p_4 N_L^2 + p_5 N_L \mu_d + p_6 \mu_d^2 . \tag{12}$$

After fitting, we get:

$$\begin{aligned} p_1 &= 3.063 \times 10^{-3} & p_2 &= 1.180 \times 10^{-2} \\ p_3 &= 7.214 \times 10^{-4} & p_4 &= -1.576 \times 10^{-3} \\ p_5 &= 1.227 \times 10^{-5} & p_6 &= -1.977 \times 10^{-6} . \end{aligned} \tag{13}$$

In (13), to avoid confusion, we omitted the units of measurement. However, we emphasize that this expression for a is valid when the carrier frequency, f_c, is expressed in GHz, the average distance between vehicles, μ_d, is in meters, and

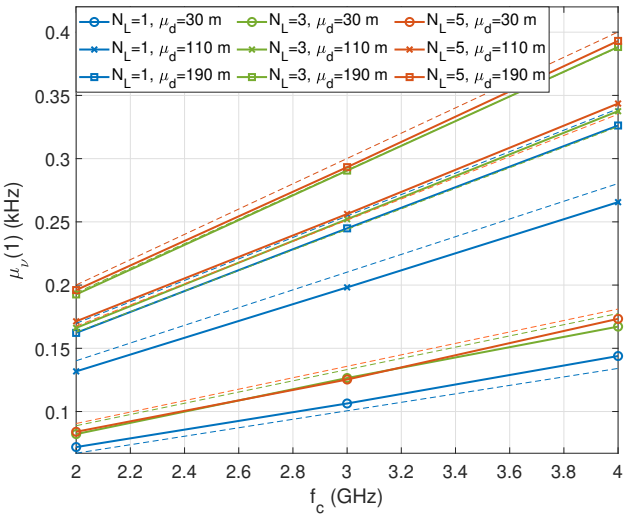

Fig. 8: Average Doppler shift of the LoS path (solid lines), fitted using the V-TDL model (dashed lines).

the Doppler shift, $\boldsymbol{\mu}_\nu(1)$, is in kHz. Dashed lines in Fig. 8 represent the modeled $\boldsymbol{\mu}_\nu(1)=af_c$, demonstrating that the V-TDL model accurately approximates the estimated curves.

Next, we consider the nLoS paths. The blue lines with circular shaped markers in Figures 9, 10 and 11, show the components of $\boldsymbol{\mu}_\nu$ as estimated in all the 27 triplets (f_c, μ_d, N_L).

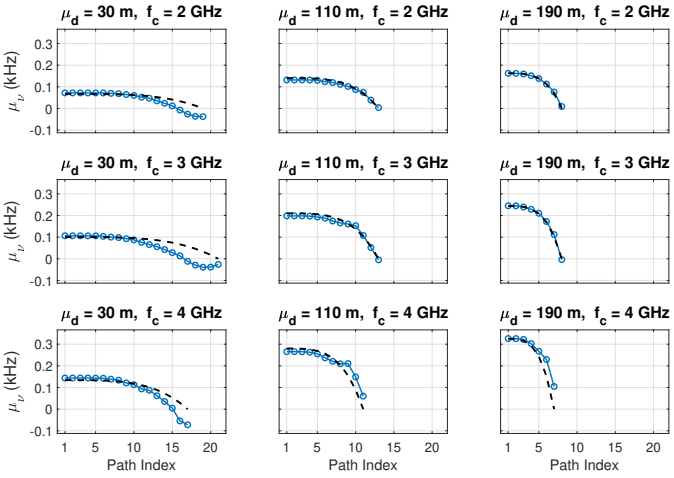

Fig. 9: Average Doppler shift across scenarios with N_L=1 (blue markers), fitted using the V-TDL model (black dashed lines).

Trying to model all the scenarios would be overly complex and impractical. Thus, we make the following approximations. First, we impose that, in all scenarios, the average Doppler shift of the P-th path is equal to 0 kHz. As shown by the results in Figures 9, 10, and 11, this assumption holds for the majority of the scenarios. Second, we assume that the derivative of all the curves is approximately zero when evaluated for the first path, which, again, is a reasonable approximation since, for the first path, the slope is negligible in all the considered scenarios.

We then model the average Doppler shift across paths using a fourth-degree polynomial of the following form:

$$f_\nu(p) \triangleq \alpha_1 p^4 + \alpha_2 p^2 + \alpha_3 \tag{14}$$

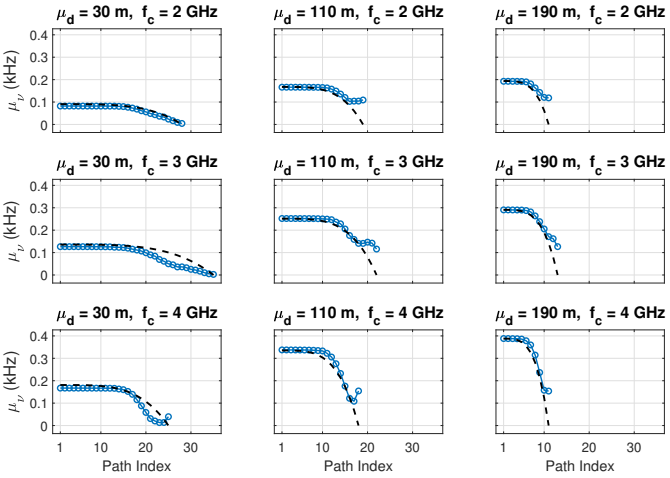

Fig. 10: Average Doppler shift across scenarios with N_L=3 (blue markers), fitted using the V-TDL model (black dashed lines).

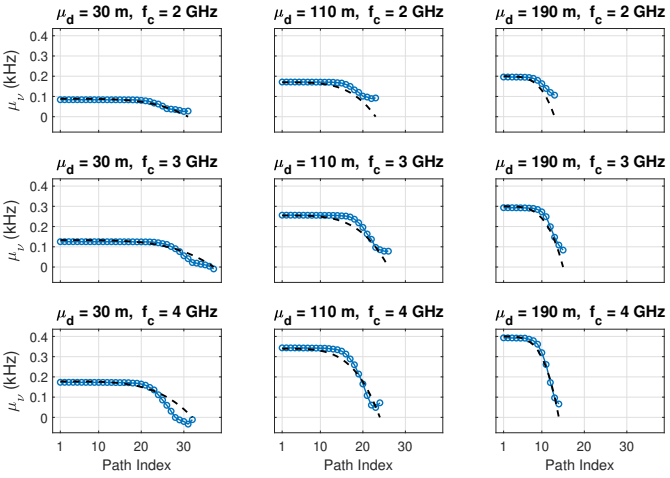

Fig. 11: Average Doppler shift across scenarios with N_L=5 (blue markers), fitted using the V-TDL model (black dashed lines).

where p=1, ..., P is the discrete path index, but in (14), it is relaxed to a continuous variable over the interval $[1, P]$ to enable curve fitting.

According to our previous observations, the polynomial coefficients must satisfy the following conditions:

$$\begin{cases} f_\nu(1)=\boldsymbol{\mu}_\nu(1) \\ f_\nu(P)=0 \\ \frac{df_\nu}{dp}\Big|_{p=1}=0 \end{cases} \tag{15}$$

which leads to the below explicit equations:

$$\begin{cases} \alpha_1+\alpha_2+\alpha_3=a\cdot f_c \\ \alpha_1 P^4+\alpha_2 P^2+\alpha_3=0 \\ 4\alpha_1+2\alpha_2=0\,. \end{cases} \tag{16}$$

If P>1, this system admits a unique solution for α_1, α_2, and

α_3, which is given by:

$$\begin{cases} \alpha_1 = \frac{-a \cdot f_c}{(P^2-1)^2} \\ \alpha_2 = \frac{2a \cdot f_c}{(P^2-1)^2} \\ \alpha_3 = \frac{a \cdot f_c \cdot P^2 \cdot (P^2-2)}{(P^2-1)^2} \,. \end{cases} \tag{17}$$

As a result, the V-TDL model expresses the average Doppler shift of the different paths as:

$$\boldsymbol{\mu}_\nu(i) = f_\nu(i), \quad i = 1, \ldots, P \tag{18}$$

with $f_\nu(p)$ computed according to (14) and (15).

Black dashed lines in Figures 9, 10, and 11 show the average Doppler component curves generated with V-TDL. When compared against the empirical estimated curves (blue markers), it is clear that we get a less accurate representation. However, our approach enables us to easily model the average Doppler shift of *all* paths given *any* triplet (f_c, μ_d, N_L) as input, while still retaining a sufficient level of accuracy.

Next, we model the covariance matrix $\boldsymbol{\Sigma}_\nu$. First, we assume that the diagonal elements are equal to the variance given by the "3σ" rule. This assumption might seem too simplistic; however, as we previously argued, what truly affects the system performance is the correlation among the different paths. The "3σ" rule ensures a probability of 0.9973 that the Doppler shift of the LoS path remains below $\nu_{\max}$, as expressed by:

$$\mathbb{P}(\boldsymbol{\mu}_\nu(1) - 3\sigma_\nu \leq \boldsymbol{\nu}_+(1) < \boldsymbol{\mu}_\nu(1) + 3\sigma_\nu) \approx 0.9973 \,. \tag{19}$$

Since $\boldsymbol{\mu}_\nu(1)$ is positive, the stricter bound to guarantee is: $\boldsymbol{\nu}_+(1) < \boldsymbol{\mu}_\nu(1) + 3\sigma_\nu$, i.e., $\nu_{\max} = \boldsymbol{\mu}_\nu(1) + 3\sigma_\nu$, which leads to:

$$\sigma_\nu = (\nu_{\max} - \boldsymbol{\mu}_\nu(1))/3 \,. \tag{20}$$

The maximum Doppler shift can be expressed as $\nu_{\max} \triangleq v^{\max}/\lambda_c$ with $v^{\max}$ being depending on the considered scenario. However, in our experiments, we set $v^{\max}$ to 160 km/h to keep it consistent with the velocity limit on highways. Also, for the sake of brevity, in our plots we present the results only for the scenarios with $N_L = 3$, as they effectively represent the overall trend. Fig. 12 (blue lines with markers) illustrates the estimated Pearson correlation coefficients between the Doppler shift of different paths and the LoS path.

The curves are well approximated by the following algebraic Sigmoid function:

$$g_\nu(p) \triangleq \frac{1}{2} - \frac{(p - \beta_2)}{\sqrt{\beta_1 + 4(p - \beta_2)^2}} \tag{21}$$

where $p = 1, \ldots, P$ denotes the path index (again relaxed to a continuous variable). Based on the behavior of the curves, we impose the following constraints:

$$\begin{cases} g_\nu(1) = 0.99 \\ g_\nu(P) = 0.01 \end{cases} \tag{22}$$

which leads to the solution:

$$\begin{cases} \beta_1 = \frac{99(P-1)^2}{2401} \\ \beta_2 = \frac{P+1}{2} \,. \end{cases} \tag{23}$$

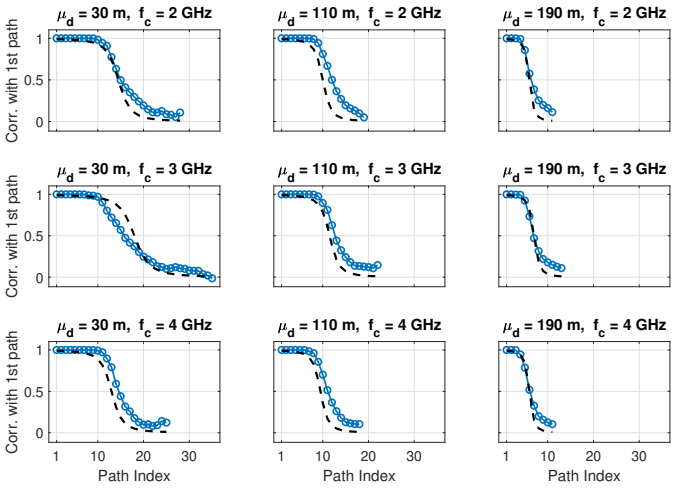

Fig. 12: Doppler shift Pearson correlation coefficient with LoS path, across scenarios with $N_L = 3$ (blue lines with markers), fitted using the V-TDL model (black dashed lines).

Fig. 12 shows (black dashed lines) the resulting approximation given by $g_\nu(p)$.

What is still missing is the correlation between paths j and k when both are different from 1, where we remind that "1" denotes the LoS path. Looking at Fig. 6, the yellow square-like shape suggests approximating their Pearson correlation as the minimum of the correlations between path j and 1 and that between path k and 1. The minimum is used because the physics of the system suggests that the highest correlation always occurs with the LoS path. In other words, multipath components j and k are correlated with each other because they are both highly correlated with the LoS component.

Then, based on the above observations, the V-TDL model expresses the covariance matrix of the Doppler shift as:

$$\boldsymbol{\Sigma}_\nu(i,j) = \begin{cases} \sigma_\nu^2 & \text{if } i = j \\ \sigma_\nu^2 \cdot g_\nu(j) & \text{if } i = 1 \wedge j > 1 \\ \sigma_\nu^2 \cdot g_\nu(i) & \text{if } i > 1 \wedge j = 1 \\ \sigma_\nu^2 \cdot \min\{g_\nu(i), g_\nu(j)\} & \text{otherwise} \end{cases} \tag{24}$$

where $i, j = 1, \ldots, P$ and $g_\nu(p)$ computed according to (21) and (23).

Finally, once $\boldsymbol{\nu}_+$ has been generated according to (11), the V-TDL model expresses the Doppler vector as:

$$\boldsymbol{\nu} \triangleq (2X - 1) \cdot \boldsymbol{\nu}_+, \quad X \sim \mathcal{B}(1/2) \tag{25}$$

where $\mathcal{B}$ denotes the Bernoulli distribution. Eq. (25) aims to account for the bimodal behavior observed in Fig. 4, where the "positive" and "negative" Gaussians have the same probability of occurrence.

C. Modeling the Number of Paths

We now model the average number of paths, $\mathbb{E}[P]$, according to the input traffic triplet (f_c, μ_d, N_L). Fig. 13 (solid lines) shows the estimated average number of paths against the average distance between vehicles, μ_d. In this analysis, we fix

the carrier frequency f_c to 3 GHz, as the effect of the carrier frequency on the number of paths is negligible.

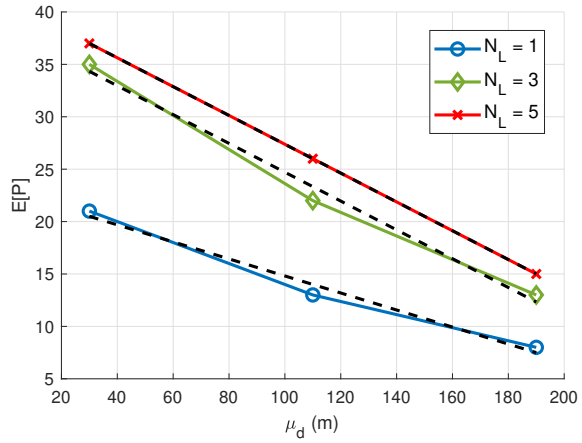

Fig. 13: Average number of paths, across scenarios with f_c=3 GHz (solid lines), fitted using the V-TDL model (black dashed lines).

Using a similar approach to the one used for modeling the Doppler shift, the V-TDL model approximates $\mathbb{E}[P]$ using the following first-degree polynomial:

$$\mathbb{E}[P]=\gamma_1 \cdot \mu_d + \gamma_2 \tag{26}$$

where γ_1 and γ_2 are given by:

$$\begin{cases} \gamma_1=0.0070 \cdot N_L^2 - 0.0563 \cdot N_L - 0.0320 \\ \gamma_2=-1.6068 \cdot N_L^2 + 14.1875 \cdot N_L + 10.3568\,. \end{cases} \tag{27}$$

The black dashed lines in Fig. 13 show that the V-TDL model accurately approximates the average number of paths for different traffic conditions. Once $\mathbb{E}[P]$ has been determined, then we set $P=\lfloor \mathbb{E}[P] \rceil$.

D. Modeling the Average Delays

The V-TDL model assigns a fixed delay to each path. Fig. 14 (blue circular markers) presents the estimated average delays for different traffic scenarios.

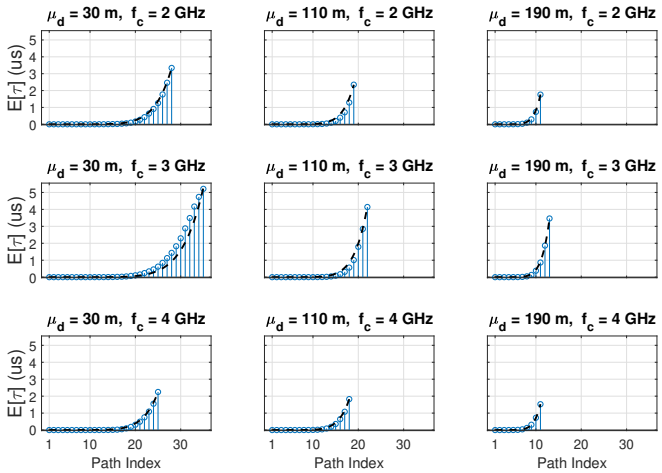

Fig. 14: Average delay across scenarios with N_L=3 (blue markers), fitted using the V-TDL model (black dashed lines).

The trend follows a power-law behavior, which we approximate using the function:

$$t_\tau(p) \triangleq \varepsilon_1 \cdot (p-1)^{\varepsilon_2} \tag{28}$$

where p=1, ..., P denotes the path index (again relaxed to a continuous variable). We impose the following two conditions:

$$\begin{cases} t_\tau(P)=\tau_{\max} \\ \frac{dt_\tau}{dp}\Big|_{p=P}=\bar{D}\frac{\tau_{\max}}{P} \end{cases} \tag{29}$$

where $\tau_{\max}$ represents the delay spread, which coincides with the delay of the last path since paths are ordered in increasing delay. The term $\bar{D}$ is the average normalized derivative, empirically estimated as 7.7601 across all 27 scenarios:

$$\bar{D} \triangleq \mathbb{E}\left[\frac{P}{\tau_{\max}}\frac{dt_\tau}{dp}\Big|_{p=P}\right]=7.7601\,. \tag{30}$$

Eq. (29) simplifies to the following explicit form:

$$\begin{cases} \varepsilon_1(P-1)^{\varepsilon_2}=\tau_{\max} \\ \varepsilon_1\varepsilon_2(P-1)^{\varepsilon_2-1}=\bar{D}\frac{\tau_{\max}}{P}\,. \end{cases} \tag{31}$$

This leads to the following solution:

$$\begin{cases} \varepsilon_1=e^{\left(P\cdot\ln(\tau_{\max})+\bar{D}\cdot(1-P)\cdot\ln(P-1)\right)/P} \\ \varepsilon_2=\bar{D}\frac{P-1}{P} \end{cases} \tag{32}$$

where the term $\tau_{\max}$ in (32) is normalized to (1 ns), to ensure that the argument of the logarithm is dimensionless.

As a result, the V-TDL model expresses the delays of the different paths as:

$$\tau_i=t_\tau(i), \quad i=1,\ldots,P \tag{33}$$

with $t_\tau(p)$ computed according to (28) and (29).

The delay spread $\tau_{\max}$ can be selected according to the specific scenario, where suggested values for typical propagation environments can be found in [46]. Fig. 14 (black dashed lines) shows the modeled delays and that V-TDL accurately approximates the estimated average delays.

E. Modeling the Average Path Power

Next, we model the average power of different paths relative to the LoS component (set at 0 dB), i.e.,

$$\mathbb{E}\left[|h_i|^2\right], \quad i=2,\ldots,P. \tag{34}$$

As the first step, we analyze the impact of traffic parameters on the average power of the 2-nd path. Fig. 15 (solid lines) illustrates the estimated $\mathbb{E}[|h_2|^2]$ for different values of f_c and μ_d. Again, due to its limited impact on the power distribution, in our results we fixed the N_L parameter to 3.

The curves can be approximated by a linear model:

$$\mathbb{E}\left[|h_2|^2\right]=b \cdot f_c + q \tag{35}$$

where the coefficients b and q are given by:

$$\begin{cases} b &= -9.60\times10^{-7}\cdot\mu_d^2 - 2.03\times10^{-5}\cdot\mu_d \\ &\quad +9.54\times10^{-2} \\ q &= 8.10\times10^{-7}\cdot\mu_d^2 + 3.45\times10^{-4}\cdot\mu_d \\ &\quad -1.20\times10^{-1}\,. \end{cases} \tag{36}$$

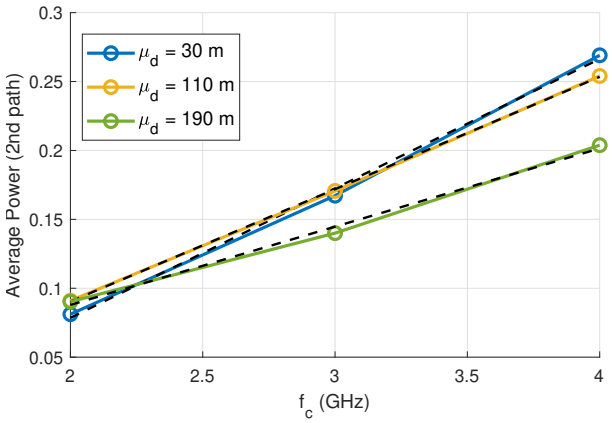

Fig. 15: Average power of the 2-nd path across scenarios with N_L=3 (lines with blue markers), fitted using the V-TDL model (black dashed lines).

Fig. 15 (black dashed lines) shows that the V-TDL model accurately approximates the average power of the 2-nd path.

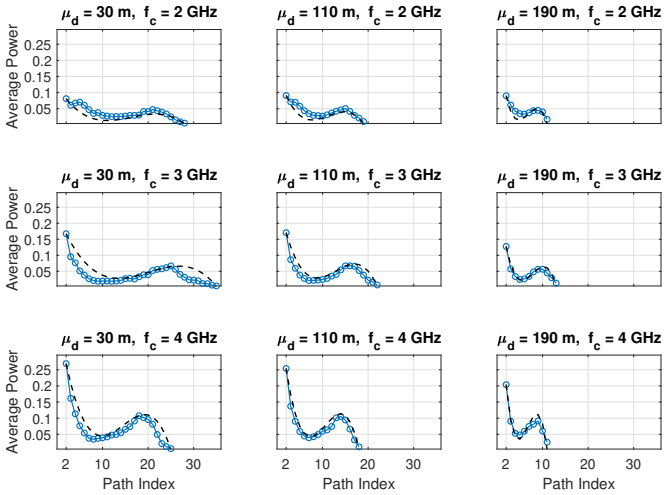

Fig. 16: Average power of different paths across scenarios with N_L=3 (blue lines with markers), fitted using the V-TDL model (black dashed lines).

Now, we extend our analysis to the remaining paths. Fig. 16 (blue lines with circular markers) illustrates the estimated average power across different paths. Such a trend can be well approximated by the following polynomial expression:

$$J(p)=z_1 \cdot p^3 + z_2 \cdot p^2 + z_3 \cdot p + z_4 \tag{37}$$

where p=2, . . . , P is the path index. The polynomial coefficients are determined by imposing the following constraints:

$$\begin{cases} J(2) = \mathbb{E}\left[|h_2|^2\right] \\ J(P) = c_0 \\ J(p_0) = \mathbb{E}\left[|h_2|^2\right] / d_0 \\ \left.\dfrac{dJ}{dp}\right|_{p=p_0} = 0 \end{cases} \tag{38}$$

where c_0=0.0032 (equivalent to −25 dB) represents a typical threshold on the dB gap in power levels between the weakest detectable path and the LoS path adopted in channel models [46]. Consistently, the highway measurement campaign in [24] reports power delay profiles that remain above −25 dB dB with respect to the LoS. The parameters p_0 and d_0 are chosen as the closest rational values that minimize the mean squared error between the estimated and modeled average path powers, resulting in $p_0 = (11/30)\cdot(P+2)$ and $d_0 = 6$. Solving the system in (38) yields the expressions shown in (39), valid for $P > 2$.

As a result, the V-TDL model expresses the average power across paths as:

$$\mathbb{E}\left[|h_i|^2\right]_{\text{dB}}=10\log_{10} J(p), \quad p=2,\ldots,P \tag{40}$$

and $\mathbb{E}\left[|h_1|^2\right]_{\text{dB}}$=0 dB. Fig. 16 (black dashed lines) illustrates the resulting average power profile (in linear scale) obtained using the V-TDL model.

F. Channel Realizations

Once all the model parameters have been computed, V-TDL can be used to generate a new channel realization for each transmitted frame. Each realization consists of P paths, each characterized by the delay τ_i, the Doppler shift ν_i, and the channel coefficient h_i for i=1, . . . , P. The number of paths and the paths delay are fixed and computed as described in Sections V-C and V-D. The Doppler shifts are drawn from the multivariate distribution outlined in Section V-B. Finally, the channel coefficients are assumed to follow a circularly symmetric complex Gaussian distribution: $h_i \sim \mathcal{CN}(0, \mathbb{E}\left[|h_i|^2\right])$, where $\mathbb{E}[|h_i|^2]$ modeled as in Section V-E. This assumes that the channel coefficients of different paths are independent, a simplification supported by the results in Fig. 7, which indicates a (small) correlation only for the first few paths.

G. Complexity

When compared to V-CORE, V-TDL exhibits very low complexity, since it does not require populating a road or computing the bistatic RCS for all reflectors. Relatively to simple TDL models such as EVA, V-TDL has instead higher complexity, mainly because of the generation of correlated Doppler shifts using the precomputed Cholesky decomposition of the covariance matrix – an operation that scales quadratically with the number of paths. However, since the number of paths in typical channel models is small, the complexity of V-TDL remains very modest, i.e., the use of V-TDL introduces just a minor overhead in the overall channel emulation process.

VI. Numerical Results

This section first compares the V-TDL model to the V-CORE and EVA models, evaluating the performance of the OFDM and OTFS modulations and analyzing the factors that lead to performance differences across the various channel models (Sec. VI-A). It then analyzes how OTFS performance is influenced by different degrees of path correlation (Sec. VI-B). Finally, it evaluates how channel diversity and OTFS performance vary with different system bandwidths (Sec. VI-C).

$$
\begin{aligned}
z_1 &= [(1-d_0)\mathcal{E}_0(P-p_0)^2 + (d_0c_0-\mathcal{E}_0)(p_0-2)^2]/(d_0D_0)\\
z_2 &= [(d_0-1)\mathcal{E}_0P^3 - 3(d_0-1)\mathcal{E}_0Pp_0^2 + (2d_0\mathcal{E}_0-2d_0c_0)p_0^3 + (6d_0c_0-6\mathcal{E}_0)p_0^2 + 8(\mathcal{E}_0-d_0c_0)]/(d_0D_0)\\
z_3 &= [2(1-d_0)\mathcal{E}_0p_0P^3 + 3(d_0-1)\mathcal{E}_0p_0^2P^2 + (-d_0\mathcal{E}_0+d_0c_0)p_0^4 + 12(\mathcal{E}_0-d_0c_0)p_0^2 - 16(\mathcal{E}_0-d_0c_0)p_0]/(d_0D_0)\\
z_4 &= [\mathcal{E}_0P^3(d_0p_0^2-4p_0+4) + \mathcal{E}_0P^2(-2d_0p_0^3+6p_0^2-8) + \mathcal{E}_0P(d_0p_0^4-12p_0^2+16p_0) - 2d_0c_0p_0^2(p_0-2)^2]/(d_0D_0)\\
&\text{where} \qquad D_0=(P-2)(P-p_0)^2(p_0-2)^2, \qquad \mathcal{E}_0=\mathbb{E}\big[|h_2|^2\big].
\end{aligned}
\tag{39}
$$

TABLE IV: Parameters for V-CORE and V-TDL

	PARAMETER	VALUE
V-CORE		
G1	Same parameters as in Table I	
G2	Number of lanes N_L	5
	$v_\ell^{\min}$	{70, 85, 100, 115, 130} km/h
	$v_\ell^{\max}$	{100, 115, 130, 145, 160} km/h
	Veh. length in each lane L_ℓ	{16.0, 6.0, 6.0, 6.0, 4.4} m
	Ave. dist. between veh. μ_d	40 m
	Safety dist. between veh. D_s	15 m
V-TDL		
G1	Number of lanes N_L	3
	Ave. dist. between veh. μ_d	80 m
	Delay Spread τ_{max}	4500 ns
	Maximum velocity $v^{\max}$	160 km/h
G2	Number of lanes N_L	5
	Ave. dist. between veh. μ_d	40 m
	Delay Spread τ_{max}	4500 ns
	Maximum velocity $v^{\max}$	160 km/h

A. OTFS vs. OFDM

We compare the OTFS and OFDM modulation schemes under (i) the proposed V-TDL model, (ii) the geometry-based stochastic model V-CORE, and (iii) the EVA model. For V-CORE and V-TDL, we consider two traffic scenarios, named G1 and G2, with the latter being more complex due to higher traffic intensity and a greater number of lanes than the former. The model parameters for both V-CORE and V-TDL are listed in Table IV, with missing parameters for V-CORE set as in Table I. The sole parameter for EVA is the maximum vehicle speed, which is set to 160 km/h.

We outline the key assumptions of our analysis below, and summarize the OFDM/OTFS parameter settings in Table V.

1) Integer Delay Values: Given a system with bandwidth B and frame duration T_{f}, the *normalized delays* and *normalized Doppler shifts* are defined as $\ell_i \triangleq \tau_i B$ and $\kappa_i \triangleq \nu_i T_{\text{f}}$, respectively. The set of distinct normalized delays is given by $\mathcal{L} = \{\ell_i : i=1,\dots,P\}$ and it is commonly assumed that $\mathcal{L}\subset\mathbb{N}$. Notice that this assumption typically does not hold for the Doppler shifts.

2) Channel Estimation: We assume that channel state information is known at the receiver. This means that the receiver has knowledge of the noise variance σ^2, the complex channel coefficients h_i, the normalized delays ℓ_i, and the normalized Doppler shifts κ_i for each path i.

In practice, the receiver cannot differentiate between physical paths that map to the same delay-Doppler bin. Consequently, two paths i and j that satisfy $\ell_i=\ell_j$ and $\lfloor\kappa_i\rceil=\lfloor\kappa_j\rceil$ are not resolvable and can be combined into a single equivalent path k with an aggregated complex gain $h_k=h_i+h_j$. The remaining distinct paths are indexed from $i=1$ to P^*, where $P^*\leq P$ represents the number of resolvable paths.

TABLE V: System parameters

PARAMETER	VALUE
Bandwidth, B	15.36 MHz
Delay bins (subcarriers), M	512
Doppler bins (time slots), N	128
Subcarrier spacing, Δf	30 kHz
Frame duration, $T_{\text{f}}=N/\Delta f$	4.2 ms
Carrier frequency, f_c	3.6 GHz
Data modulation	4-QAM (uncoded)

3) Geometric Channel Coherence Time: We assume that the delay-Doppler channel response remains constant over the duration of an entire frame. As outlined before, with $M=512$ and $\Delta f=30$ kHz, the path length resolution of the system is $c/(M\Delta f)\approx 19.5$ m. If $N=128$, the total frame duration is $T_{\text{f}}=N/\Delta f=4.3$ ms. Under these conditions, a vehicle moving at 160 km/h travels less than 0.2 m during one frame, which is significantly below the system path length resolution. This indicates that the frame duration is shorter than the geometric coherence time, allowing both the delay and the Doppler to be considered constant over the entire frame – a key assumption for the application of OTFS.

4) Signal-to-Noise Ratio: The average SNR is defined as:

$$
\overline{\text{SNR}} = \frac{E_s}{\sigma^2}\mathbb{E}\big[\|\boldsymbol{h}\|^2\big], \qquad \|\boldsymbol{h}\|^2 = \sum_{i=1}^{P^*}|h_i|^2 \tag{41}
$$

where E_s denotes the average symbol energy. Since the considered channel models are subject to random fading, the SNR varies from frame to frame. The definition of the average SNR in (41) aligns with that of a multiple-input single-output (MISO) system when using maximum-ratio transmission (MRT) precoding [47, Ch. 3]. Similarly, in OTFS, MRC ensures the coherent combination of multipath components, achieving an analogous gain.

5) Detection: As discussed in Section III, we employ minimum mean square error (MMSE) single-tap equalization for OFDM and delay-time MRC detection for OTFS.

Fig. 17 illustrates the performance in terms of Frame Error Rate (FER) versus the average SNR, where a frame is considered erroneous if at least one bit within the frame is received incorrectly. Notice that OTFS outperforms OFDM under all considered models and scenarios. Concerning the EVA model, OTFS gains approximately 5 dB over both V-CORE and V-TDL. In fact, as highlighted in the previous

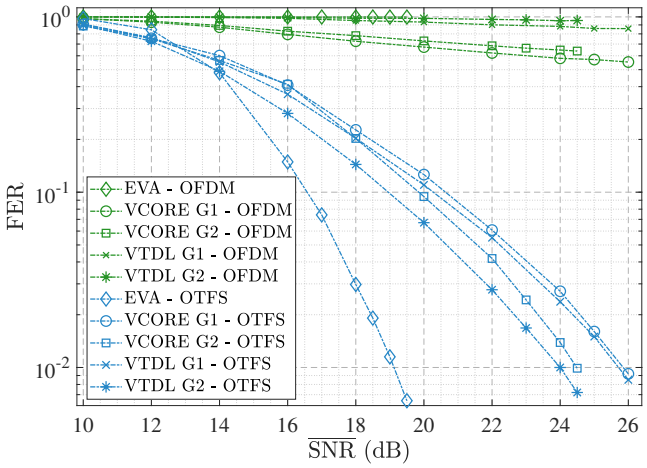

Fig. 17: FER vs. $\overline{\text{SNR}}$: Comparison between OFDM and OTFS under the V-CORE and V-TDL models in different scenarios, and the EVA model.

sections, EVA considers the different taps to be completely independent, and as a consequence, the channel diversity is increased. However, geometry-based simulations under V-CORE show high correlations between propagation paths, mainly due to the road geometry extending predominantly along the horizontal direction. As previously observed, this causes multiple paths originating from surrounding vehicles to fall into the same bin, thereby reducing channel diversity. Furthermore, the V-CORE power-delay profile (characterized by the bistatic RCS of reflective vehicles) decays more rapidly than the EVA one. As a result of the above considerations, the EVA model overestimates OTFS performance in high-speed vehicular scenarios.

Conversely, the proposed V-TDL in G1 and G2 is able to closely approximate the OTFS performance of the corresponding G1 and G2 scenarios under the V-CORE model, where OTFS performs better in G2 than in G1 due to the higher traffic intensity, which leads to greater diversity. We recall that V-TDL, unlike V-CORE, uses a fixed number of paths. While this may introduce some bias during the collection of statistics, the similar system performance observed under both models indicates that fixing the number of paths does not significantly reduce the fidelity of the performance evaluation.

The simulation results show that our V-TDL model effectively captures the typical correlation in vehicular propagation environments, distinguishing different levels of channel diversity based on traffic intensity. This variation is then reflected in the OTFS performance across the different scenarios.

Also, it is interesting to observe that OFDM exhibits exactly the opposite trend across the different channel models and scenarios: unlike OTFS, the more diversity there is, the more OFDM struggles with ICI.

B. OTFS Performance under Different Correlation Levels

One of the main features of the proposed V-TDL model is that it captures the correlation between multipath components, which unavoidably degrades the performance of the OTFS system. To further investigate how correlation affects OTFS performance, we propose three slightly modified versions of the original EVA channel model (denoted as EVA-1, EVA-2, and EVA-3), where we introduce different degrees of correlation between the multipath components. Specifically, in EVA-1 the paths are fully independent as for EVA, but the Doppler shifts are distributed according to the marginal distributions of the Doppler shifts of the first nine paths of the V-TDL model in G1. EVA-2 is the same as EVA-1, except that the path delays are scaled by a factor of two, thus only increasing the correlation between the path delays. EVA-3 is identical to EVA-2, except that the Doppler shifts follow the joint distribution of the first nine paths of the V-TDL model in G1, including the off-diagonal covariance terms; therefore, both the path delays and the Doppler shifts are correlated. All three models share the same power delay profile as EVA.

In the following, we compare the OTFS system (Table V) performance under the three new variants of the EVA model. Results are shown in Fig. 18. EVA-1 performs similarly to the original EVA model, indicating that the specific Doppler shift distribution is not critical; rather, what matters is that the paths are uncorrelated. EVA-2 loses approximately 2 dB with respect to EVA-1, and EVA-3 experiences a similar loss relative to EVA-2. These results confirm that increasing correlation among multipath components degrades OTFS performance.

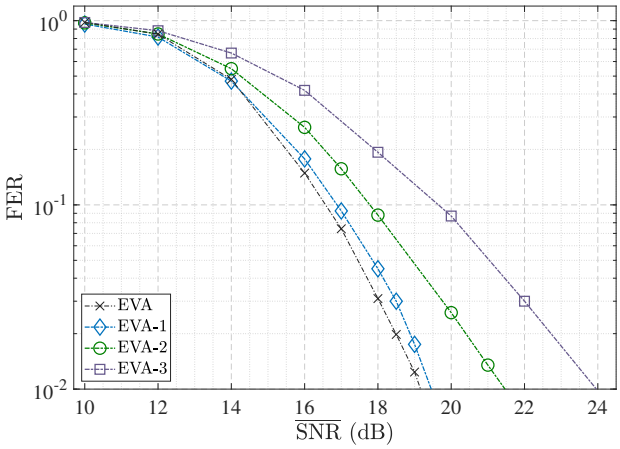

Fig. 18: FER vs. $\overline{\text{SNR}}$: OTFS under the EVA model with different levels of correlation among paths.

C. OTFS Performance under Different System Bandwidths

Another important factor that affects channel diversity is delay resolution, which is inversely proportional to system bandwidth $B{=}M\Delta f$. In this analysis, we compare the OTFS performance under the EVA model and the V-TDL model in scenario G1, while varying the system bandwidth. We test three different configurations $M{=}32, 128, 512$, keeping all other parameters as in Table V. To ensure a fair comparison, we cannot consider the Frame Error Rate, since different values of M lead to different frame sizes when N is fixed. Therefore, we measure the OTFS Symbol Error Rate (SER),

i.e., the error rate of the rows in the delay-Doppler domain matrix $\mathbf{X}_{\text{dd}}$, whose size N is fixed across the three bandwidth settings. Results are shown in Fig. 19, demonstrating that for lower bandwidth values, OTFS performance decreases due to the reduced delay resolution of the receiver, which translates into lower perceived channel diversity.

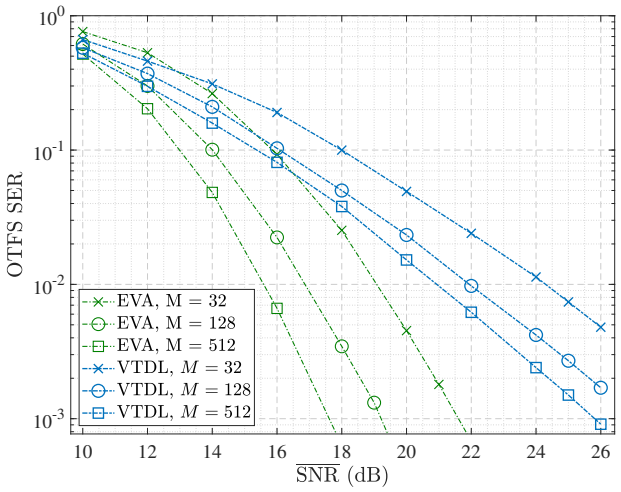

Fig. 19: OTFS SER vs. $\overline{\text{SNR}}$: OTFS under EVA and V-TDL model in G1 with different values of system bandwidth.

VII. Conclusion and Future Works

We proposed the vehicular tapped delay-line (V-TDL) channel model, designed to accurately capture the dynamics of high-speed vehicular environments. The V-TDL model combines the simplicity of fixed-tap models with a precise statistical representation of key parameters such as delays, Doppler shifts, and channel gains. Our results demonstrate that V-TDL achieves the same level of accuracy as a – much more complex – ray-tracing-based model. Importantly, unlike existing stochastic models, which assume independent taps and tend to overestimate performance, our model captures the correlation between multipath components. This is a very relevant feature of the proposed model, as such a correlation can lead to a significant variation of the communication system performance. We highlighted how the system bandwidth affects the channel diversity perceived by the receiver, thereby impacting OTFS performance. Nevertheless, our results show that OTFS outperforms OFDM in all considered vehicular scenarios, particularly in environments with high traffic intensity and large delay spreads, which enhance channel diversity.

Our study paves the way for several research directions that can be pursued to further improve the proposed model. These include: (i) considering a wider variety of bistatic RCS measurements, for instance by incorporating diverse vehicle shapes and varying elevation angles between the transmitter and receiver antennas; and (ii) extending the model to account for fractional delays. Furthermore, since our results highlight the significance of path correlation, it would be valuable to investigate how this correlation can be exploited in the design of novel detection algorithms for OTFS systems.

References

[1] C.-X. Wang and et al., "On the road to 6G: Visions, requirements, key technologies, and testbeds," *IEEE Comm. Surveys & Tutorials*, vol. 25, no. 2, pp. 905–974, 2023.

[2] W. Saad, M. Bennis, and M. Chen, "A vision of 6G wireless systems: Applications, trends, technologies, and open research problems," *IEEE Network*, vol. 34, no. 3, pp. 134–142, 2020.

[3] M. Giordani, M. Polese, M. Mezzavilla, S. Rangan, and M. Zorzi, "Toward 6G networks: Use cases and technologies," *IEEE Communications Magazine*, vol. 58, no. 3, pp. 55–61, 2020.

[4] J. Wu and P. Fan, "A survey on high mobility wireless communications: Challenges, opportunities and solutions," *IEEE Access*, vol. 4, pp. 450–476, 2016.

[5] M. Noor-A-Rahim, Z. Liu, H. Lee, M. O. Khyam, J. He, D. Pesch, K. Moessner, W. Saad, and H. V. Poor, "6G for vehicle-to-everything (V2X) communications: Enabling technologies, challenges, and opportunities," *Proceedings of the IEEE*, vol. 110, no. 6, pp. 712–734, 2022.

[6] S. Hakak, T. R. Gadekallu, P. K. R. Maddikunta, S. P. Ramu, M. Parimala, C. De Alwis, and M. Liyanage, "Autonomous vehicles in 5G and beyond: A survey," *Vehicular Communications*, vol. 39, p. 100551, 2023. [Online]. Available: https://www.sciencedirect.com/science/article/pii/S2214209622000985

[7] D. Tse and P. Viswanath, *Fundamentals of Wireless Communication*. Cambridge University Press, 2005.

[8] 3GPP, "Evolved Universal Terrestrial Radio Access (E-UTRA); User Equipment (UE) Radio Transmission and Reception," Technical Specification Group Radio Access Network, Tech. Rep. TS 36.101.

[9] ITU, "Rec. ITU-R m.1034-1: Requirements for the radio interface(s) for international mobile telecommunications-2000," 1997.

[10] A. Compagnoni, R. Tuninato, C. F. Chiasserini, R. Garello, A. Nordio, and E. Viterbo, "OTFS vs. OFDM in High-speed Vehicular Traffic Scenarios," in *IEEE WCNC*. IEEE, 2025.

[11] K. Schaubach, N. Davis, and T. Rappaport, "A ray tracing method for predicting path loss and delay spread in microcellular environments," in *1992 Proceedings VTS Conference*, pp. 932–935.

[12] D. He, B. Ai, K. Guan, L. Wang, Z. Zhong, and T. Kürner, "The design and applications of high-performance ray-tracing simulation platform for 5G and beyond wireless communications: A tutorial," *IEEE Communications Surveys & Tutorials*, vol. 21, no. 1, pp. 10–27, 2019.

[13] K. Guan, H. Yi, D. He, B. Ai, and Z. Zhong, "Towards 6G: Paradigm of realistic terahertz channel modeling," *China Communications*, vol. 18, no. 5, pp. 1–18, 2021.

[14] R. Hadani, S. Rakib, M. Tsatsanis, A. Monk, A. J. Goldsmith, A. F. Molisch, and R. Calderbank, "Orthogonal Time Frequency Space Modulation," in *IEEE WCNC*, 2017, pp. 1–6.

[15] T. Wang, J. Proakis, E. Masry, and J. Zeidler, "Performance Degradation of OFDM Systems due to Doppler Spreading," *IEEE Trans. on Wireless Communications*, vol. 5, no. 6, pp. 1422–1432, 2006.

[16] H. Groll and et al., "Sparsity in the delay-doppler domain for measured 60 GHz vehicle-to-infrastructure communication channels," in *IEEE ICC Workshops*, 2019, pp. 1–6.

[17] Y. Ma, G. Ma, N. Wang, Z. Zhong, and B. Ai, "OTFS-TSMA for massive internet of things in high-speed railway," *IEEE Trans. on Wireless Communications*, vol. 21, no. 1, pp. 519–531, 2022.

[18] L. Gaudio, G. Colavolpe, and G. Caire, "OTFS vs. OFDM in the presence of sparsity: A fair comparison," *IEEE Trans. on Wireless Communications*, vol. 21, no. 6, pp. 4410–4423, 2022.

[19] M. K. Ramachandran, G. D. Surabhi, and A. Chockalingam, "OTFS: A new modulation scheme for high-mobility use cases," *J. of the Indian Institute of Science*, vol. 100, pp. 315–336, 2020. [Online]. Available: https://doi.org/10.1007/s41745-020-00167-4

[20] P. Raviteja, E. Viterbo, and Y. Hong, "OTFS performance on static multipath channels," *IEEE Wireless Communications Letters*, vol. 8, no. 3, pp. 745–748, 2019.

[21] K. R. Murali and A. Chockalingam, "On OTFS Modulation for High-Doppler Fading Channels," in *ITA*, 2018, pp. 1–10.

[22] P. Priya, Y. Hong, and E. Viterbo, "OTFS channel estimation and detection for channels with very large delay spread," *IEEE Trans. on Wireless Communications*, vol. 23, no. 9, pp. 11 920–11 930, 2024.

[23] Y. Hong, T. Thaj, and E. Viterbo, *Delay-Doppler Communications Principles and Applications*. AP-Elsevier, London, UK, Feb. 2022.

[24] A. Paier, J. Karedal, N. Czink *et al.*, "Characterization of vehicle-to-vehicle radio channels from measurements at 5.2 GHz," *Wireless Personal Communications*, vol. 50, no. 1, pp. 19–32, 2009.

[25] F. Wiffen, L. Sayer, M. Z. Bocus, A. Doufexi, and A. Nix, "Comparison of OTFS and OFDM in Ray Launched sub-6 GHz and mmWave Line-of-Sight Mobility Channels," in *IEEE PIMRC*, 2018, pp. 73–79.

[26] L. Xiong, Z. Yao, H. Miao, and B. Ai, "Vehicle-to-vehicle channel characterization based on ray-tracing for urban road scenarios," *Wireless Communications and Mobile Computing*, vol. 2021, no. 1, p. 8854247, 2021.

[27] J. Nuckelt, T. Abbas, F. Tufvesson, C. Mecklenbrauker, L. Bernado, and T. Kurner, "Comparison of ray tracing and channel-sounder measurements for vehicular communications," in *2013 IEEE 77th Vehicular Technology Conference (VTC Spring)*, 2013, pp. 1–5.

[28] J. Karedal, F. Tufvesson, N. Czink, A. Paier, C. Dumard, T. Zemen, C. F. Mecklenbrauker, and A. F. Molisch, "A Geometry-Based Stochastic MIMO Model for Vehicle-to-Vehicle Communications," *IEEE Trans. on Wireless Communications*, vol. 8, no. 7, pp. 3646–3657, 2009.

[29] R. T. Rakesh and E. Viterbo, "Geometry Based Stochastic Channel Modeling using Ambit Processes," in *IEEE WCNC*, 2020, pp. 1–6.

[30] F. M. Alsalami, Z. Ahmad, O. Haas, and S. Rajbhandari, "Regular-shaped geometry-based stochastic model for vehicle-to-vehicle visible light communication channel," in *2019 IEEE Jordan International Joint Conference on Electrical Engineering and Information Technology (JEEIT)*, 2019, pp. 297–301.

[31] Y. Yuan, C.-X. Wang, X. Cheng, B. Ai, and D. I. Laurenson, "Novel 3D geometry-based stochastic models for non-isotropic mimo vehicle-to-vehicle channels," *IEEE Trans. on Wireless Communications*, vol. 13, no. 1, pp. 298–309, 2014.

[32] S. Beygi, E. G. Ström, and U. Mitra, "Geometry-based stochastic modeling and estimation of vehicle to vehicle channels," in *IEEE ICASSP*, 2014, pp. 4289–4293.

[33] Q. Deng, Y. Ge, and Z. Ding, "A unifying view of OTFS and its many variants," *IEEE Communications Surveys & Tutorials*, pp. 1–1, 2025.

[34] T. Blazek, H. Groll, S. Pratschner, and E. Zochmann, "Vehicular Channel Characterization in Orthogonal Time-Frequency Space," in *IEEE ICC Workshops*, 2019, pp. 1–5.

[35] D. Radovic, C. F. Mecklenbräuker, and T. Blazek, "Otfs performance over different measured vehicular 60 ghz millimeter-wave channels," in *2021 International Conference on Software, Telecommunications and Computer Networks (SoftCOM)*, 2021, pp. 1–5.

[36] R. Marsalek, J. Blumenstein, J. Vychodil, T. Mikulasek, P. Jung, and A. Pfadler, "Real-world otfs channel estimation performance evaluation on mmwave vehicular channels," in *2024 27th International Workshop on Smart Antennas (WSA)*, 2024, pp. 1–7.

[37] P. Singh, A. Gupta, H. B. Mishra, and R. Budhiraja, "Low-complexity ZF/MMSE MIMO-OTFS receivers for high-speed vehicular communication," *IEEE Open J. of the Comm. Soc.*, vol. 3, pp. 209–227, 2022.

[38] C. S. Reddy, P. Priya, D. Sen, and C. Singhal, "Spectral efficient modem design with OTFS modulation for vehicular-iot system," *IEEE Internet of Things Journal*, vol. 10, no. 3, pp. 2444–2458, 2023.

[39] Y. Ge, Q. Deng, D. G. G., Y. L. Guan, and Z. Ding, "OTFS signaling for SCMA with coordinated multi-point vehicle communications," *IEEE Trans. on Vehicular Technology*, vol. 72, no. 7, pp. 9044–9057, 2023.

[40] P. Raviteja, Y. Hong, E. Viterbo, and E. Biglieri, "Practical pulse-shaping waveforms for reduced-cyclic-prefix OTFS," *IEEE Trans. on Vehicular Technology*, vol. 68, no. 1, pp. 957–961, 2019.

[41] T. Thaj and E. Viterbo, "Low Complexity Iterative Rake Decision Feedback Equalizer for Zero-Padded OTFS Systems," *IEEE Trans. on Vehicular Technology*, vol. 69, no. 12, pp. 15 606–15 622, 2020.

[42] N. J. Willis, *Bistatic Radar*, ser. Radar, Sonar and Navigation. Institution of Engineering and Technology, 2004. [Online]. Available: https://digital-library.theiet.org/content/books/ra/sbra003e

[43] S. Rao, D. Wilton, and A. Glisson, "Electromagnetic Scattering by Surfaces of Arbitrary Shape," *IEEE Trans. on Antennas and Propagation*, vol. 30, no. 3, pp. 409–418, 1982.

[44] Naval Air Warfare Center Weapons Div Point Mugu, CA, Avionics Department Code, 450000E, *Electronic Warfare and Radar Systems Engineering Handbook*, 4th ed., Sep. 2013.

[45] G. Acosta, K. Tokuda, and M. A. Ingram, "Measured joint doppler-delay power profiles for vehicle-to-vehicle communications at 2.4 ghz," in *IEEE Global Telecommunications Conference, 2004. GLOBECOM'04.*, vol. 6. IEEE, 2004, pp. 3813–3817.

[46] 3GPP, "Study on channel model for frequencies from 0.5 to 100 GHz," 3GPP, Tech. Rep., 2024.

[47] E. Björnson and Özlem Tuğfe Demir, *Introduction to Multiple Antenna Communications and Reconfigurable Surfaces*. Boston-Delft: Now Publishers, 2024. [Online]. Available: http://dx.doi.org/10.1561/9781638283157